

## Article

# Analysis of Vortex Evolution in the Runner Area of Water Pump Turbine under Runaway Conditions

Feng Zhou <sup>1,2</sup>, Qifei Li <sup>2,\*</sup> and Lu Xin <sup>2</sup><sup>1</sup> Key Laboratory of Solar Power System Engineering, Jiuquan 735000, China; 202085800139@lut.edu.cn<sup>2</sup> School of Energy and Power Engineering, Lanzhou University of Technology, Lanzhou 730050, China; 221080703001@lut.edu.cn

\* Correspondence: lqfy@lut.cn

**Abstract:** In order to study the evolution principle of the coherent structure in the low flow rate runaway condition, the pump turbine of a certain pumped storage power plant was employed. The transient dynamic stress of the runner was numerically simulated and examined in this study in order to analyze the coherent structure of the vortex and the stability of the grid connection during the transition process. Based on the realizable  $k-\varepsilon$  turbulent model, the unsteady flow of the whole pump turbine channels was calculated. The results show that the flow in the runner channels presents with a turbulence state, and with many different scales vortices. These vortex structures are mainly distributed in the inlet region of the blade, the area of the blade trailing edge and the middle section of the runner channels. These vortex structures affect the distribution of the blade pressure load. Moreover, the vortex structure at the inlet of the runner depends on the change in the attack angle. In the flow region formed at the outlet of the blade near the suction surface and the runner cone, the blade has a limited effect on the fluid; thus, the vortex structure depends on the Coriolis force and the centrifugal force joint action. The evolution of these vortex structures will have a greater impact on the grid connection of the power station. During the operation of the power station, it is necessary to reduce the time of transitional conditions so that the power station can operate efficiently.

**Keywords:** pump turbine; runaway condition; coherent structure; channel vortices; numerical simulation

**Citation:** Zhou, F.; Li, Q.; Xin, L.Analysis of Vortex Evolution in the Runner Area of Water Pump Turbine under Runaway Conditions. *Processes* **2023**, *11*, 2080. <https://doi.org/10.3390/pr11072080>

Academic Editor: Krzysztof Rogowski

Received: 8 June 2023

Revised: 4 July 2023

Accepted: 6 July 2023

Published: 12 July 2023



**Copyright:** © 2023 by the authors. Licensee MDPI, Basel, Switzerland. This article is an open access article distributed under the terms and conditions of the Creative Commons Attribution (CC BY) license (<https://creativecommons.org/licenses/by/4.0/>).

## 1. Introduction

Since the carbon peak target of 2030 and the carbon neutral vision of 2060 were proposed [1], the large-scale grid connection of new energy sources and the construction of new power systems have become an inevitable trend in the development of energy and power systems, while, in the current energy structure, pumped storage power plants play a unique and irreplaceable role in grid peaking, regulating energy structure, irrigation and tourism [2–7], so accelerating the development of pumped storage is an inevitable choice and an effective way to guarantee energy and power security.

Pump turbines need to switch quickly between pumping and generation modes so as to ensure the stability of the grid frequency and the standard orderly distribution of power [8]. However, under the transition conditions between pump mode and energy mode, fluid inertial instabilities such as water hammering, vibration and stalling can occur due to the change in flow pattern inside the pump turbine and the redistribution of velocity in each fluid domain [9–12]. These vortices consume the kinetic energy of the fluid and, in interaction with each other, seriously affect the efficiency and operational stability of the equipment. For example, Wang [13] studied the internal flow mechanism of the pump turbine braking condition and anti-pump condition through numerical calculation and proposed that the impeller area reflux and vortex in the non-leaf area are the main causes of high-amplitude and low-frequency pressure pulsation; Zhang [14] studied the pressure pulsation in the S area of a pump turbine based on a combination of experimental and

numerical calculation methods of the pressure pulsation in the S zone of the water pump turbine and concluded that the pressure pulsation in the tail pipe of the water pump turbine is related to the vortex zone of the tail pipe; Li [15] accurately calculated the flow characteristics of the water pump turbine under turbine operating conditions by means of the separation vortex model and found that, as the flow rate decreases, the flow separation phenomenon occurs in the leaf grille region and gradually evolves into a large-scale vortex that blocks the flow channel and has a deteriorating effect on the flow stability; Widmer et al. [16] found that the average convective acceleration in the guide vane channel and the ability of vortex formation to rotate are responsible for determining whether the stationary vortex and stall rotation are initially the same, both of which can cause instability in the unit; Klemm D [17] performed a dynamic numerical simulation of the flow regime of a water pump turbine under flyaway conditions with the help of CFD to improve the flyaway no-load stability by varying the opening rate of the guide vane, where it was found that, by reducing the opening rate of the guide vane, the occurrence of fly-away no-load instability could be reduced effectively, and it was also found that the no-load instability was more severe at the low head than at the high head and that the destabilization was more serious than that of high-head water; and Xu [18] applied a combination of numerical calculation and particle image velocimetry of the full characteristic test to study the flow state in the S characteristic region of the pump turbine, analyzed the influence of the guide vane opening on the vortices inside the flow channel under low flow conditions and obtained that, as the guide vane opening decreases, the number of vortices in the impeller channel increases, and a relatively complete high-speed water blocking ring appears between the movable guide vane, causing unstable flow. Although much research has been carried out in the industry on the unsteady flow caused by vortices inside the pump turbine, the internal flow mechanism of the pump turbine during its movement in the S characteristic zone has not yet been fully grasped, which hinders the further development of the pump turbine.

The unstable flow phenomenon caused by internal vortices is more prominent in water pump turbines under runaway conditions, the interaction between vortices of various scales and the influence mechanism of vortex motion on the mainstream is more complicated and the efficiency and operational stability of the unit are significantly reduced, so the study of the vortex evolution process under runaway conditions has more engineering significance. With the rapid development of computer technology, numerical calculations have gradually become an important tool for studying complex fluid flows, which visualize the internal flow characteristics in detail and provide an intuitive reference basis [19,20]. Therefore, this paper uses a combination of verification tests and numerical calculations to study the influence of the guide vane opening on the vortex evolution and motion process in the runner region under the runaway condition of a water pump turbine, and elucidates the vortex evolution mechanism in the relative static position of the blades and the impeller runner. This study provides theoretical references for improving the safety and stability of water pump turbines.

## 2. Materials and Methods

In this study, the mixed-flow pump turbine model was used as the research object. Considering that the internal flow in the runner region shows asymmetric characteristics under runaway conditions, a full-flow channel numerical calculation of the pump turbine is required, where the model structure is illustrated in Figure 1 and the model parameters are given by Table 1. The three-dimensional model was spatially discretized using the commercial software TurboGrid hexahedral mesh, and the boundary layer was encrypted for the blade. Worm casing and guide vane wall positions and the rated operating point of the hydraulic turbine operating condition (speed  $n = 920$  r/min, flow rate  $Q_v = 0.35$  m<sup>3</sup>/s, efficiency  $\eta = 92\%$ , head  $H = 30$  m) were used to verify the mesh irrelevance, and when the mesh number is greater than 5,575,139, the fluctuation in the hydraulic turbine efficiency is within 2%, which meets the calculation requirements; thus, the grid number of 5,575,139 was selected for numerical calculation [21,22]. Figure 2a shows the grid model diagram,

Figure 2b shows the distribution of  $y^+$  values defined at this grid size and the number of grids for each part is shown in Table 2. The min angle is calculated as the minimum internal angle of each grid cell; the higher the value, the better the grid quality. The min quality measures the mesh, and the min value is considered as the mesh quality. Grid irrelevance analysis is shown in Figure 3.

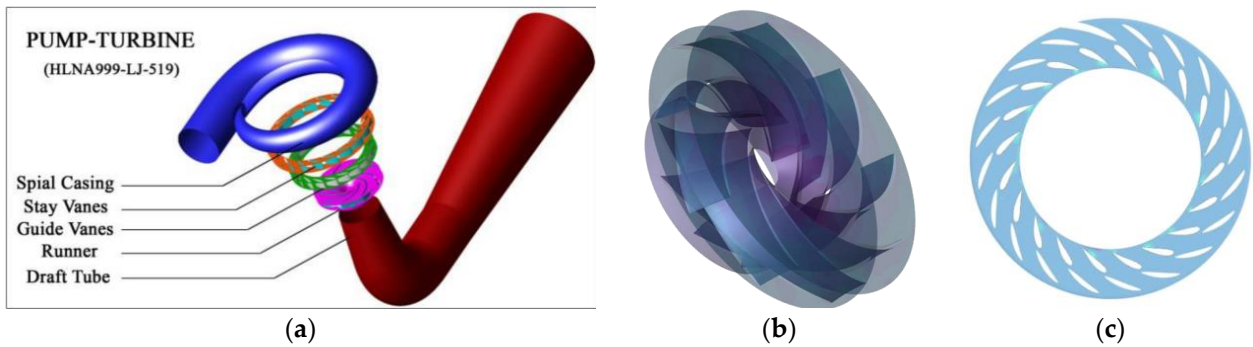


Figure 1. Computational domain of pump turbine model. (a) Pump turbine full basin model; (b) schematic diagram of the rotor water body model; (c) guide vane wing-type water body diagram.

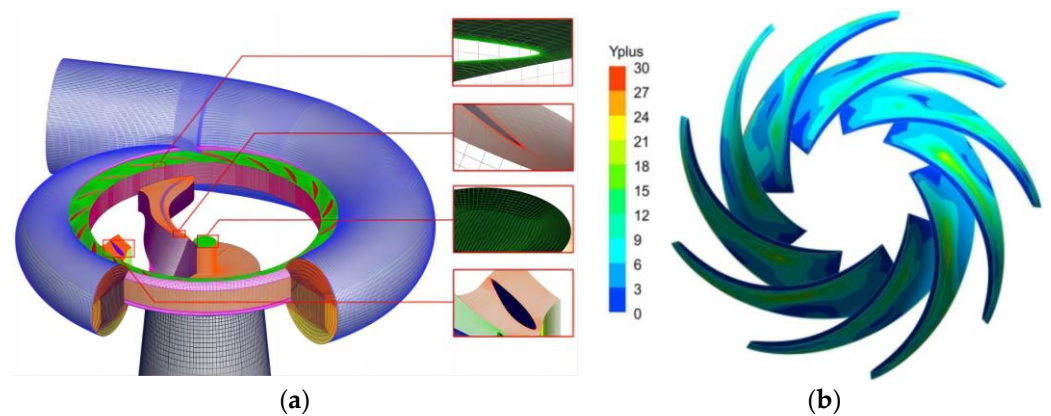


Figure 2. Mesh pattern of model pump turbine. (a) Whole configuration mesh; (b)  $Y^+$  distribution of blade.

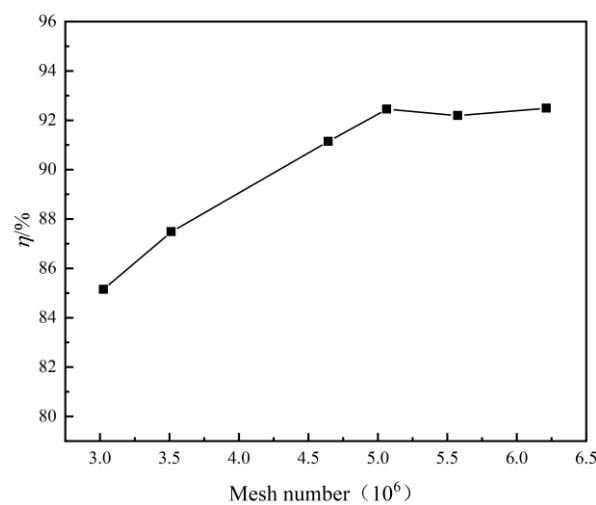


Figure 3. Grid irrelevance verification.

**Table 1.** The geometry parameters of the pump turbine.

Parameter	Symbol	Value
Diameter of the high-pressure side of the runner/mm	$D_1$	473.6
Diameter of the low-pressure side of the runner/mm	$D_2$	300
Runner blade number	$Z_r$	9
Guide vane number	$Z_g$	20
Stay vane number	$Z_s$	20
Outlet diameter of draft tube /mm	$D_{1m}$	660
Inlet diameter of volute/mm	$D_{2m}$	315
Guide vane height/mm	$b_0$	66.72
Case wrap angle/(°)	$\varphi_0$	343

**Table 2.** The grid division of each part.

Parameter	Spiral Casing and Stay Vane Number	Guide Vane	Runner	Draft Tube
Total elements	1,794,767	1,118,500	1,205,507	1,456,365
Total nodes	316,840	1,028,400	1,127,820	1,422,144
Min angle/(°)	18	29	30	36
Min quality	0.50	0.48	0.50	0.65

In this paper, the entire computational model was simulated numerically using the commercial software ANSYS FLUENT. Although the flow is strongly nonlinear in the pump turbine, the Knudsen number is still much less than one, so the flow field satisfies the assumption of velocity nonlinearity, and the fluid is considered continuous. Using the finite volume method to solve the Reynolds-average Navier–Stokes equations [23] (as Equation (1)), the realizable k- $\epsilon$  turbulence model can effectively simulate shear flows, including jet, mixed and separated flows [24–26]; thus, this paper used the realizable k- $\epsilon$  turbulence equations [23] (Equations (2) and (3)), the continuity equation [23] (Equation (4)) and Reynolds time-averaged equations to achieve a closed solvable control equation, with the mass inflow port and pressure outlet as the boundary conditions, assuming no slip on the wall. Using the runner region as the rotor region and the worm shell runner as the stator region, the steady-state calculation was solved by the multiple coordinate system method, and the transient was solved by a slip grid. The time spent for each 1° rotation of the runner blade was set as a time step to 0.00018 s.

$$\frac{\partial(\rho u_i)}{\partial t} + \frac{\partial(\rho \overline{u_i u_j})}{\partial x_j} = -\frac{\partial p}{x_i} + \frac{\partial}{\partial x_j} \left( \mu \frac{\partial u_i}{\partial x_j} - \rho \overline{u_i' u_j'} \right) + S_i \quad (1)$$

$$\frac{\partial \rho}{\partial t} + \frac{\partial(\rho u)}{\partial x} + \frac{\partial(\rho v)}{\partial y} + \frac{\partial(\rho w)}{\partial z} = 0 \quad (2)$$

$$\frac{\partial(\rho k)}{\partial t} + \frac{\partial(\rho k u_i)}{\partial x_i} = \frac{\partial}{\partial x_j} \left[ \left( \mu + \frac{\mu_t}{\sigma_k} \right) \frac{\partial k}{\partial x_j} \right] + G_k - \rho \epsilon \quad (3)$$

$$\frac{\partial(\rho \epsilon)}{\partial t} + \frac{\partial(\rho \epsilon u_i)}{\partial x_i} = \frac{\partial}{\partial x_j} \left[ \left( \mu + \frac{\mu_t}{\sigma_\epsilon} \right) \frac{\partial \epsilon}{\partial x_j} \right] + \rho C_1 E \epsilon - \rho C_2 \frac{\epsilon^2}{k + \sqrt{v \epsilon}} - \rho \epsilon \quad (4)$$

A validation test was carried out using the experimental platform of the State Key Laboratory of Hydropower Equipment (Harbin Institute of Large Electric Machinery), where the test head  $H_m = 30$  m was determined by measuring the differential pressure between the inlet and outlet [27,28]. Figures 4 and 5 show the schematic diagram and the test site of the test rig, which is a closed loop system and can operate in both directions. The maximum head allowed in the test stand was 190 m and the maximum mass flow rate was 2.0 m<sup>3</sup>/s. The small flow rate is defined as the flow rate below the rated condition

during the pump turbine operation. Figure 6 shows the  $Q_{11}$  (unit flow rate)- $n_{11}$  (unit speed) curve of the pump turbine in the transition process under different guide vane openings, where the working condition point when the rotating torque is zero is determined by a torque meter, the rotating torque at zero for each guide vane opening is the intersection of the connecting line with the  $Q_{11}$ - $n_{11}$  curve, which is the fly-away condition point, and the fly-away condition points at guide vane openings of 11, 19, 21, 25, 33, 41 and 45 mm are used as the numerical calculation conditions. The operating parameters of each calculation condition are shown in Table 3. Figure 7 compares the  $Q_{11}$ - $n_{11}$  curves of the experimental results with the numerical results. As can be seen from the figure, the numerical results match the experimental results at each working condition, and the correctness of the numerical results can be verified. Equations (5) and (6) give the calculation method of  $Q_{11}$  and  $n_{11}$ .

$$n_{11} = \frac{nD_2}{\sqrt{H}} \quad (5)$$

$$Q_{11} = \frac{Q}{D_2^2\sqrt{H}} \quad (6)$$

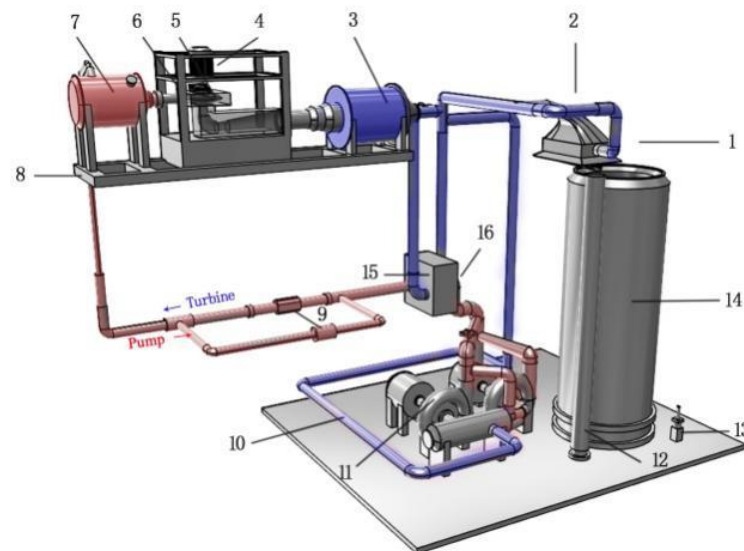


**Figure 4.** Schematic diagram of the test bed. (1. Flow board diverter; 2. nozzle; 3. low-pressure vessel; 4. dynamometer motor; 5. torque measurement system; 6. pump turbine model; 7. high-pressure vessel; 8. stent; 9. flowmeter; 10. closed system pipeline; 11. pump turbine; 12. open system pipeline; 13. weighing sensor; 14. weighing cylinder; 15. water cooling system; 16. commutation pipeline).



**Figure 5.** Test site.

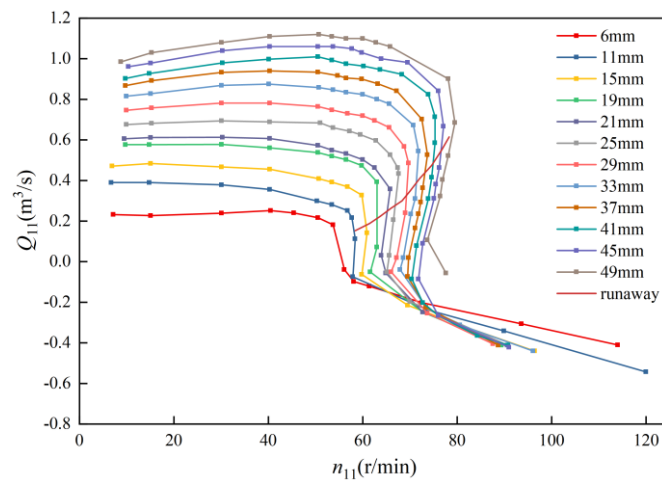


**Figure 6.** External characteristic curves under different guide vane openings (test results).

**Table 3.** Numerical simulation results of steady flow.

	$a_0/\text{mm}$	$n_{11}/(\text{r}/\text{min})$	$Q_{11}/(\text{m}^3/\text{s})$	$n/(\text{r}/\text{min})$	$q_m/(\text{kg}/\text{s})$
P1	11	57.61	0.150	1051.810	73.943
P2	19	62.30	0.215	1137.436	105.984
P3	21	64.74	0.249	1182.015	122.690
P4	25	66.26	0.276	1209.762	135.835
P5	33	70.82	0.376	1292.989	185.349
P6	41	74.47	0.511	1359.595	251.952
P7	45	76.52	0.545	1397.056	268.658

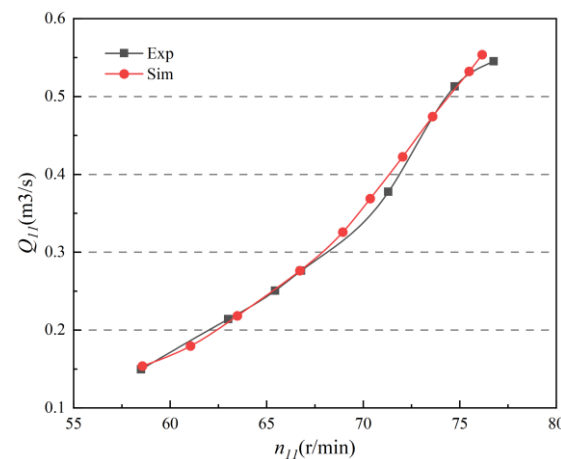


**Figure 7.** The numerical results are compared with the experimental results.

### 3. Results

Under the runaway condition, a vortex with different scales is distributed in the runner region, and the vortex with different scales in each flow passage forms coherent structures with different scales. In order to study the evolution of a coherent structure more clearly, channels were divided, as shown in Figure 8, and the rotation angle of the channel region was corrected to ensure that each runner position is relatively stationary. Figure 8 shows the unsteady numerical results of the runner region at the P1 operating point. No. 1–9 refer to the flow line distribution in different impeller runner channels at time  $t = 0.4240$  s, 0.4294 s, 0.4348 s, 0.4402 s, 0.4456 s, 0.4510 s and 0.4564 s, respectively. At these moments, the vortex appears in the middle of the blade. The position of the vortex in the image was calibrated with a red circle. In addition, it can be seen from Figure 8 that the eddy coherent

structure is also found at the inlet and outlet of the blade. Therefore, the eddy coherent structure can be divided into three parts according to their distribution positions: blade outlet, blade inlet and middle of blade passage.

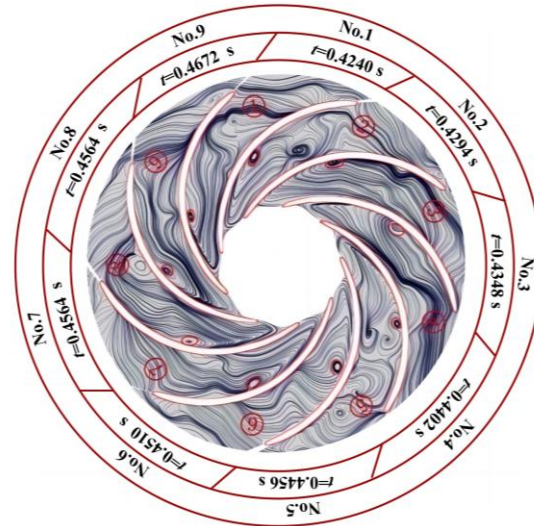


**Figure 8.** Vortex distribution in different impeller runner channels at different time.

### 3.1. Evolution of the Coherent Structure at the Blade Outlet

In order to further study the evolution rule of the coherent structure at the outlet of the blade, the streamline chart of the one channel was selected as shown in Figure 9. It shows that the coherent structure moves along the wall from the outlet of the channel to the middle with stretching and contraction. Because the fluid element in the instantaneous state of each point can be decomposed into three directions, they are the translation and expansion along the principal axis (it can be decomposed for the uniform expansion and pure deformation) and the rigid rotation around an axis. The fluid element is subjected to the maximum tension (positive in the flow direction) in the direction of  $\pi/4$  with the wall surface, and the maximum contraction force in the direction of  $3\pi/4$ . Because of the velocity difference at the trailing edge position, the flow field is subjected to shearing action, and the adhesion condition makes it generate vorticity. At the same time, it is accompanied by translation and stretching along the wall in the  $\pi/4$  direction.

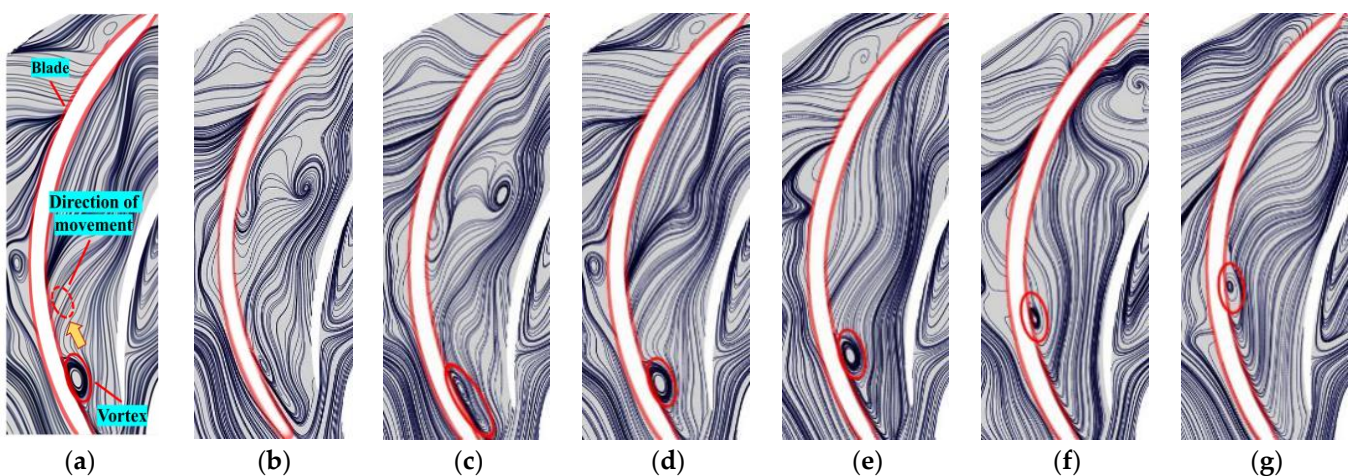


**Figure 9.** Channel (No. 1 blade channel) snapshot of the evolution of the vortex in one cycle (a):  $t = 0.4240$  s; (b):  $t = 0.4294$  s; (c):  $t = 0.4348$  s; (d):  $t = 0.4402$  s; (e):  $t = 0.4456$  s; (f):  $t = 0.4510$  s; (g):  $t = 0.4564$  s.

### 3.2. Influence of Vortex Structure at Blade Suction Side on Blade Pressure Load

Taking the No. 2 blade as the research object, the relationship between the evolution process of a vortex-dependent structure and pressure load was studied. Figure 10 indicates that the pressure load on the suction side of the blade decreases along the direction of the blade inlet and the peaks appear at the inlet and outlet of the blade, respectively, shown as Figure 11. A local high-pressure area and local low-pressure area appear in the blade outlet section, respectively. With the development of the vortex cycle, the peak position of the local high-pressure area does not change, and the position of the local low-pressure area moves towards the inlet of the blade with time corresponding to the vortex movement on the suction side of the blade. Compared to the change in the minimum low pressure in the local low-pressure area with time, local low pressure does not exist in the initial vortex stage (Figure 10a). Local low-pressure areas appear at corresponding positions with the moving blade loads of vortices. The minimum pressure value in the low-pressure area decreases, and the low-pressure area becomes more apparent. As time goes on, the position of the low-pressure area moves toward the blade inlet, and the minimum pressure gradually increases. The low-pressure area gradually becomes less noticeable and disappears with the disappearance of the vortex movement. This indicates that the vortex changes the pressure load distribution of the runner blade during the development process. Low pressure is generated locally at the vortex development location of the runner blade and the location of the low-pressure area changes with the displacement and intensity of the vortex. Compared to the local low-pressure area, the location of the local high-pressure area and the peak value do not change.

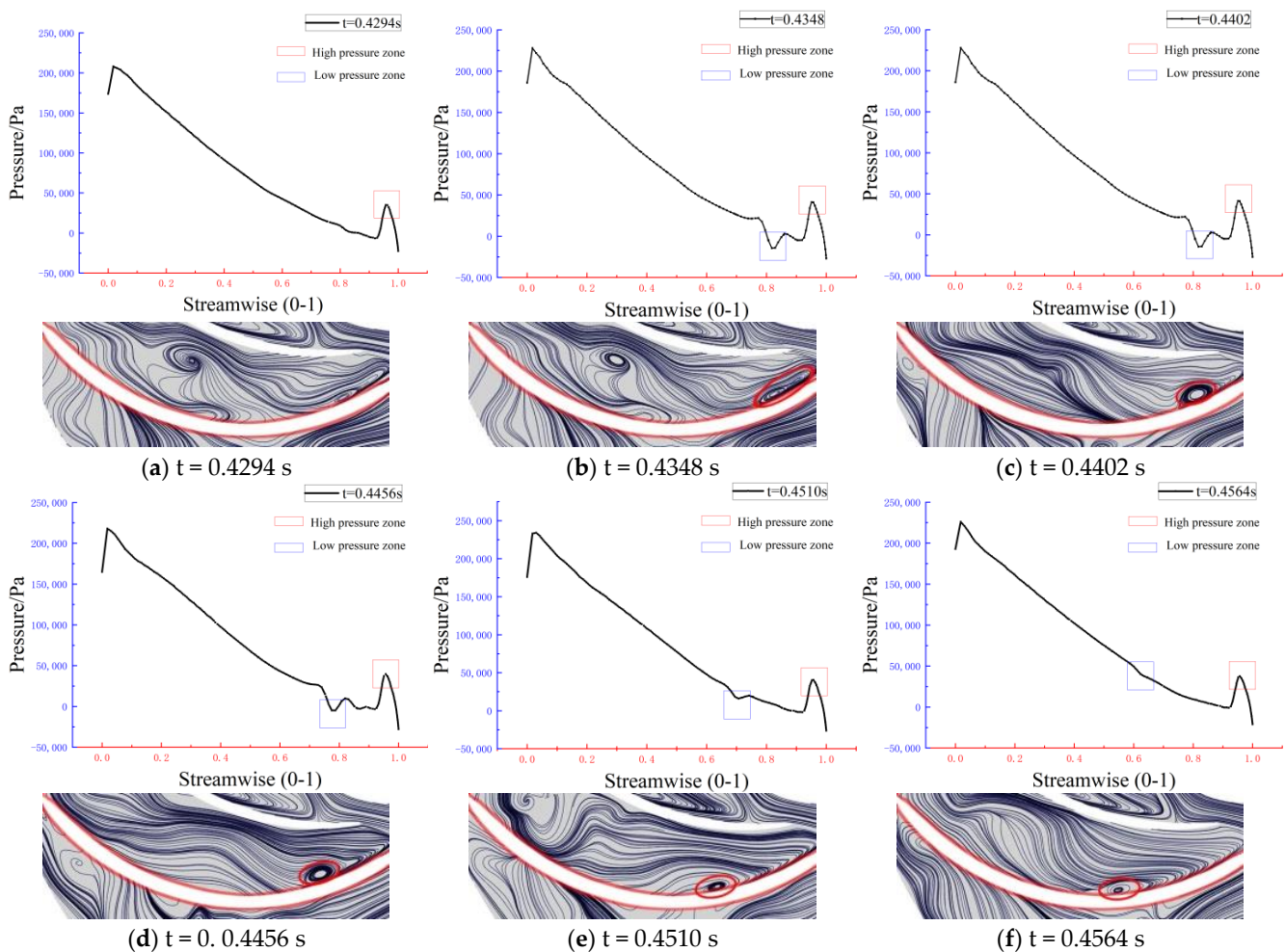
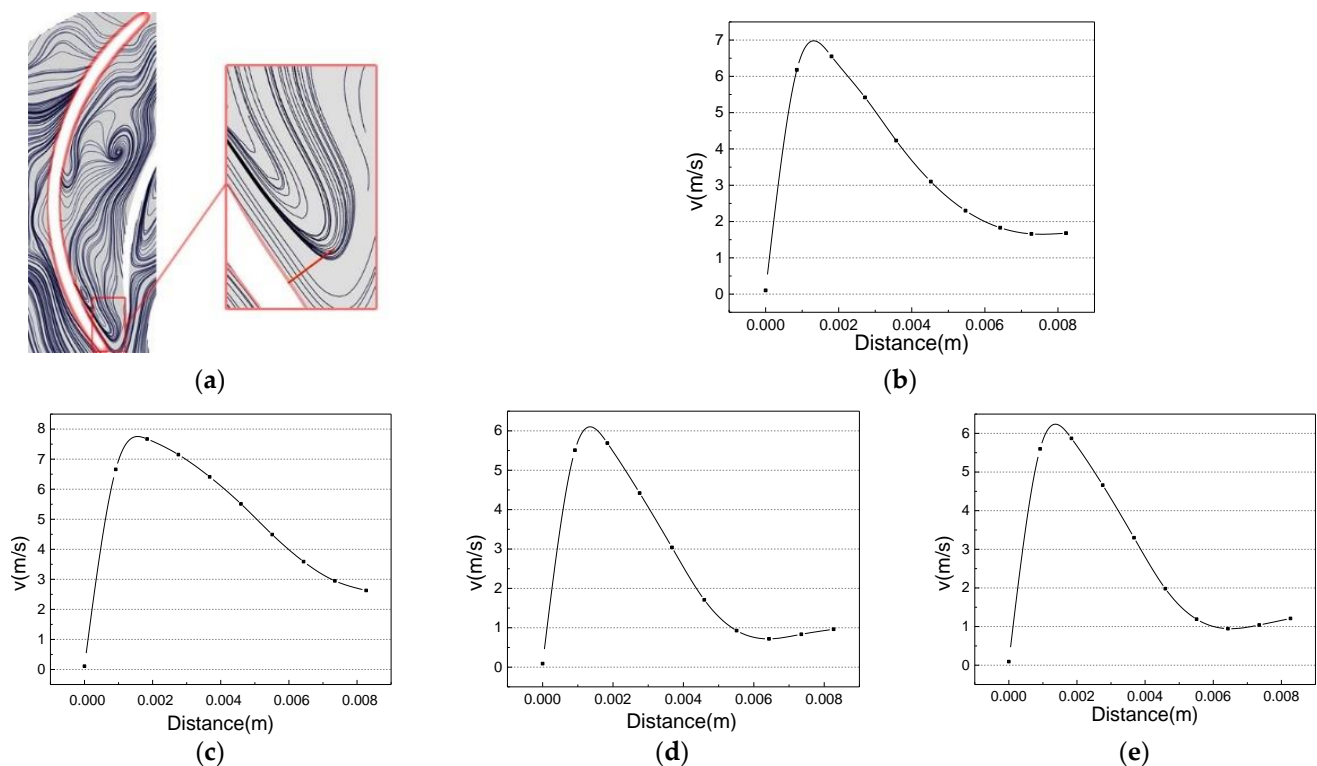


Figure 10. Blade pressure load distribution.



**Figure 11.** Tangential velocity distribution: (a) velocity extraction position; (b–e) velocity distribution on monitoring channels numbered 1, 3, 6, 9.

In order to obtain the evolution process and characteristics of the coherent structure on the suction surface of the blade, a tangential velocity distribution map was made at the birth position and time of the vortex, as shown in Figure 11.

From the tangential velocity distribution of Figure 11b, we can discover that the effect of the fluid on the outlet of the blade is determined by the shear flow. It is a flow pattern similar to a wall jet, judging from the law of velocity distribution. As shown in Figure 12, it can be found that the jet is mainly caused by the large angular velocity of the runner and the sizeable centrifugal force. With the action of centrifugal force, a high-speed rotating fluid is accumulated at the outlet position of the runner blade. The collision between a fluid and a high-speed rotating blade forces it to divert at the exit of the blade. As the speed of the runner is larger, the process of the collision between the fluid and the blade is more similar to the wall jet. Thus, a coherent structure is generated at the outlet position of the runner blade.

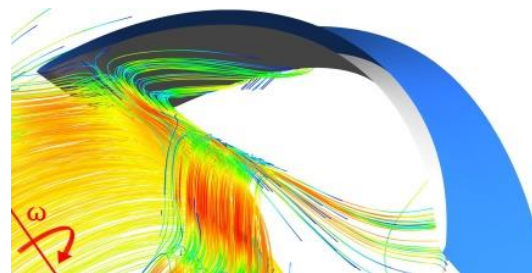


**Figure 12.** Streamline at the outlet of blade.

From the three-dimensional shape of the vorticity iso-surface in Figure 13, it can be found that the direction of the vortex and the flowing fluid are perpendicular. Thus, it can be judged that the coherent structure of the rear surface of the rotor blade is a spanwise

vortex. This is due to the effect of wall jet shearing on the uneven velocity distribution. When the disturbing wave number is sufficiently large, the shear layer is destabilized, and vorticity is formed. The inducing effect of the vortex sheet and its further enhancement with the disturbance of the flow from the blade channel make the unstable wave gradually roll up and develop into a periodic spanwise vortex. Since the vorticity of the feed fluid increases parallel to the wall, the vortex moves along the wall surface under the effect of tangential force, and the fluid velocity of the near-wall decreases with an increase in the moving distance. At the same time, due to the influence of the flow from the blade channel, the vortex core is not evenly distributed in the circumferential direction, and the vortex develops to disappear in the middle of the blade.

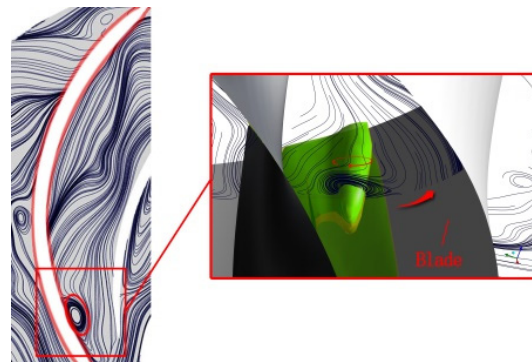


**Figure 13.** Blade spanwise vorticity structure.

### 3.3. Evolution of Coherent Structure at the Inlet of the Blade

In order to study the effect of the inlet of the blade on the flow pattern and the coherent structure of the blade, CFD-POST post-processing software was used to turbo-process the runner area under the runaway speed operating condition. From Figure 14, it is found that the vortex moves downstream and then falls, and that the process of evolution forms a vortex street. In order to clarify the evolution of morphology vortices and their causes, the No. 1 flow channel was used to show the velocity streamline diagram, as shown in Figure 14. The vortex begins at the leading edge of the blade inlet, as shown in Figure 15a. Due to the lift acting, the vortex moves backward along the leading edge of the blade and diffuses into the fluid interior. As the vortex diffuses into the fluid, external disturbances and self-induction of the main vortex cause the vortex layer to stretch, diffuse and dissipate. A twice-separation vortex was induced, as shown in Figure 15e. The concentrated vortex forms after vortex separation causes a large pressure gradient, which causes the bottom pressure to decrease. The vortex layer in the higher pressure area near the side of the blade wall is pulled into the wake to form a new vortex, and the vortex layer continues to stretch. The vortex layer is stretched, diffused or even pulled off. Finally, the vortices alternately fall off.

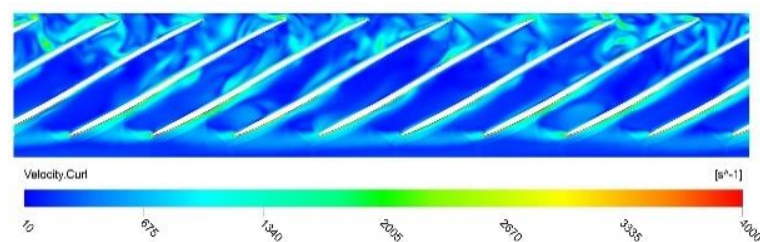


**Figure 14.** Vorticity contour of blade channels.

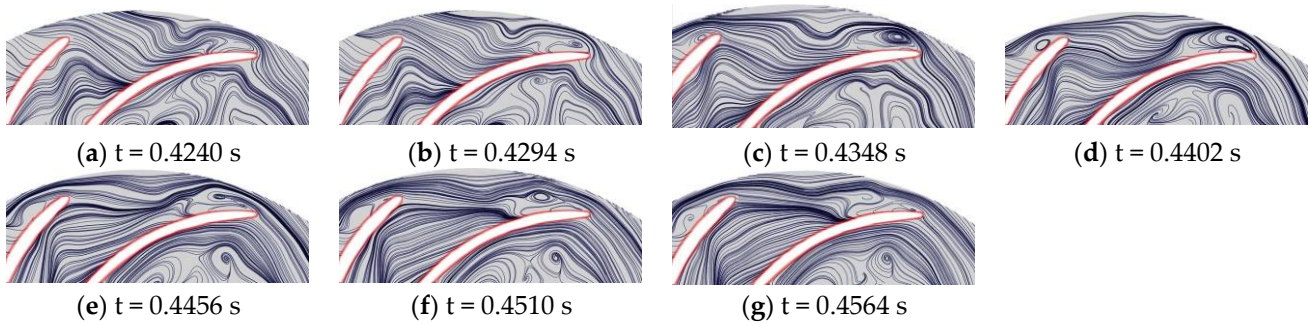


**Figure 15.** Streamline of inlet of blade.

To explore the cause of vortices at the inlet of the blade, the attack angle was calculated. According to the contour of the blade, the hydrofoil bone line was drawn, and the velocity was extracted in the vertical direction of the bone line, as shown in Figure 16a. Its attack angle was calculated, as shown in Figure 16b. From Figure 16c, it can be found that the value of the attack angle is larger. The maximum is  $22.5^\circ$  and the minimum is  $15.6^\circ$ ; in the direction from point C to point D, the attack angle first decreases and then increases. Through the calculation of other channels and conditions, the value of the attack angle is large in each case. Thus, the detailed distribution of the absolute attack angle is shown in Figure 16c–e. The distribution is irregular, and no obvious periodicity can be observed. However, it is certain that the large attack angle is responsible for the formation of vortices at the channel inlet.

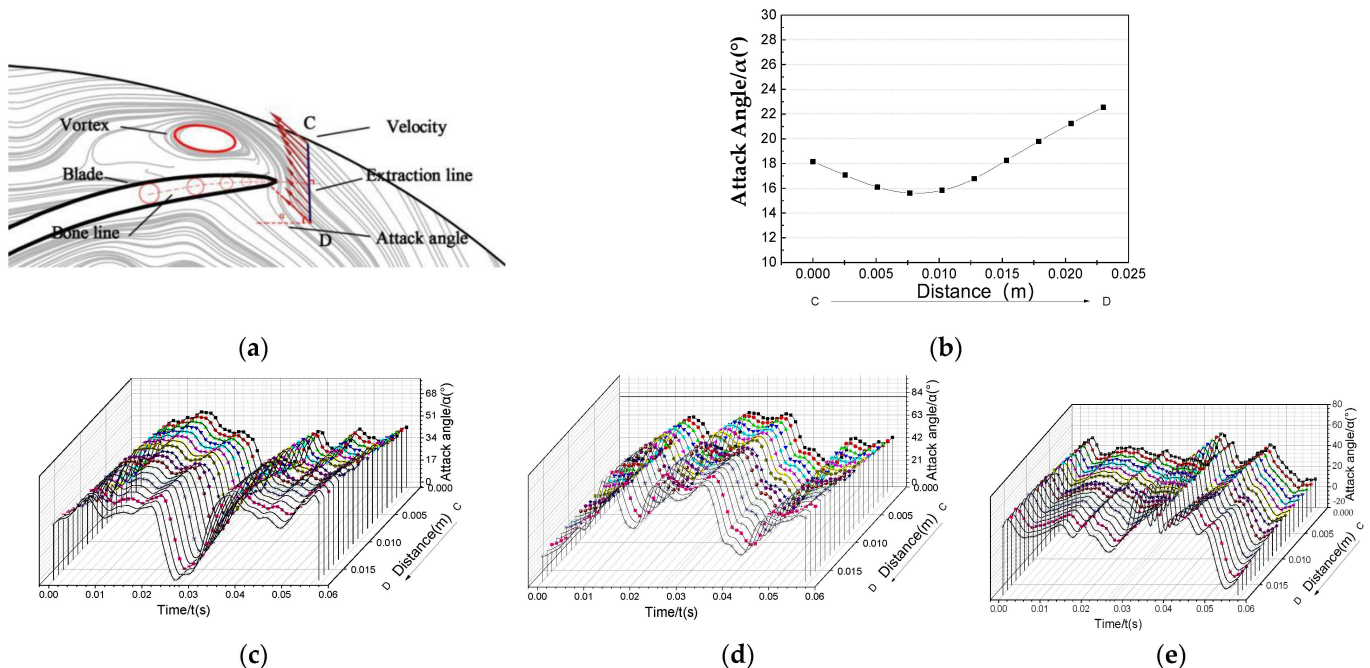


**Figure 16.** Distribution of attack angle: (a) the calculation method and position of the angle of attack; (b) the trend of the attack angle from point C to point D; (c–e) angle of attack distribution of runner No. 3, 6 and 9.

### 3.4. Evolution of Coherent Structures in a Runner Channel

In runaway conditions, different scale vortices are distributed in the middle of the runner channel. In order to study its origin and evolution, the coherent structure of the No. 7 runner channel was studied as shown in Figure 16.

Figure 17 show that the formation of the coherent structure in the middle of the channel is related to the disturbance of the incoming flow at the leading edge of the inlet

end of the blade and the jet formed by the impact of the outlet end of the blade and the fluid. As shown in Figure 17a, the leaflet flow at No. 2 is affected by the leading edge of the blade, the free shear layer is destabilized and the vortex structure at No. 2 in Figure 17b is developed and formed. At the same time, the coherent structure developed along the wall surface of the blade near the exit of the blade continues to develop upstream as shown in Figure 17b No. 1. With the vortex at No. 1 gradually approaching the vortex at No. 2, the vortex layer at position No. 3 is changed to generate a vortex structure, as shown in the position of No. 3 in Figure 17c. With the development of the structures of No. 1 and No. 3, the vortex at No. 4 is disturbed by the vortex layers. Thus, the vortices at No. 4 and No. 1 form a vertical pair, and the vortices at No. 2 and No. 3 form a vertical pair, as shown in Figure 17d. As the vortex at No. 1 continues to develop upstream of the runner, the vortex at No. 4 is “captured” by the No. 1 vortex, and the vortex at No. 1 gains a vortex that is opposite to its own vorticity, counteracting its own vorticity, as shown in Figure 17e. Due to the disturbance and self-induction between the vortex layers, the vortices at the No. 1 and No. 3 positions are destabilized and collapsed, and the runner channels return to the original flow state again, as shown in Figure 17f,g. The main reason for the formation of the coherent structure in the middle of the leaf passage is that the vortex at the No. 1 position moves along the upstream vortex of the blade and the disturbance of the incoming flow from the leading edge of the blade inlet.

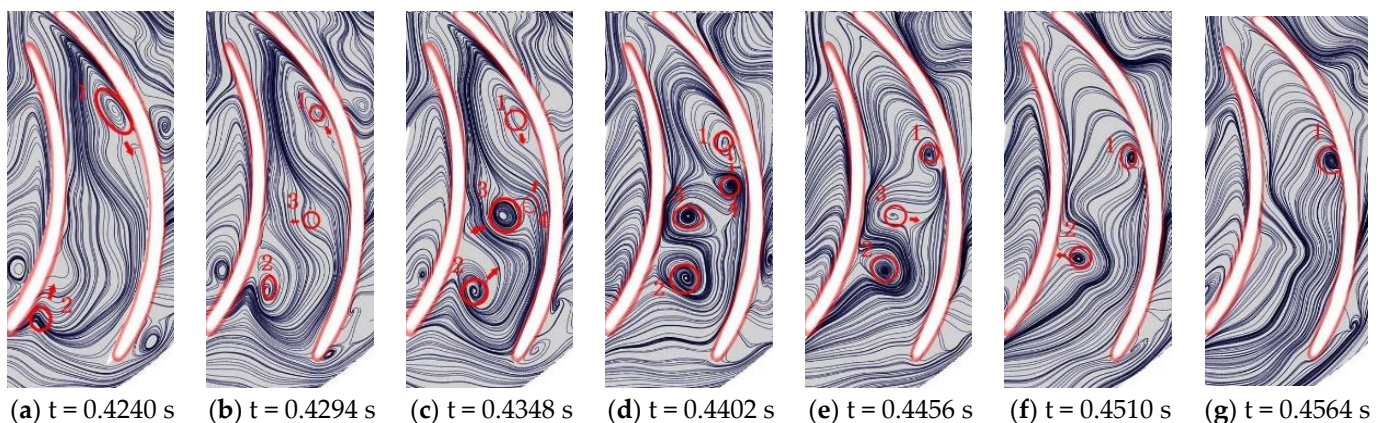


**Figure 17.** Evolution of coherent structure in the middle of the blade channel.

#### 4. Discussion

The pump turbine needs to be converted under different working conditions while operating. When the water pump turbine discharges the load, the unit may quickly enter the flyaway state under the extreme working condition of the guide vane control of the unit. The study of this problem is of great engineering significance because the flyaway transition process is a great danger to the safe and reliable operation of the unit.

In this paper, the pump turbine of a pumped storage power plant was taken as the research object, and the influence of the change in the guide vane opening on the vortex in the runner area under the flyaway condition was carefully analyzed. It was found that the result of the joint action of the angle of attack of the incoming flow and the centrifugal force determines the vortex structure in the flow channel. The evolution of the vortex process can significantly affect the grid connection of the power plant, so it is necessary to reduce the flyaway and even the whole transition process during the operation of the power plant to facilitate the long and stable operation of the pumped storage power plant. This paper provides some theoretical reference for the future research of other transition processes in pump turbines; the generation and development of a vortex in the blade runners can be predicted appropriately and also provide directions for hydraulically optimizing the design of other angle-of-attack variations, such as guide vanes and even runner blades.

There are some limitations to this work. For example, in the flyaway condition, the influence of the change in the opening degree of the guide vanes on the vortex development, the vibration and even the energy in the tailpipe region was investigated. At the same time, the transition process of the pump turbine is complex and variable. The vortex evolution and the angle of attack of the inlet flow have not formed a systematic, regular pattern.

## 5. Conclusions

The vortex-induced flow instability of the pump turbine under the flyaway condition is the key to the safe and reliable operation of the unit. This paper analyzed the evolution of the vortex coherent structure in the runner region by combining numerical analysis and experimental verification, and reached the following conclusions:

1. Under the runaway condition, the vortex coherent structure at the rotor blade tends to move along the impeller outlet to the center of the flow channel and is accompanied by stretching and contraction phenomena. The fluid element and the wall are subjected to the maximum expansion force in the  $\pi/4$  direction (flow direction is positive) and the maximum contraction force in the  $3\pi/4$  direction.
2. The pressure load on the suction surface of the blade decreases along the blade inlet direction, and a positive peak appears at the outlet; the coherent structure of the vortex has a certain influence on the phenomenon, where, with the evolution of the vortex coherent structure, the negative peak appears at the rear end of the positive peak; the location of the negative peak relates to the evolution process of the vortex coherent structure, where the location of the negative peak moves with the vortex location; the location of the positive peak does not influence the vortex location.
3. The velocity distribution of the blade angle of attack between 15.6 and 22.5 degrees was studied, and the results show that the large angle of attack is the main cause of the vortex formation, and that the vortex is formed at the leading edge of the blade, then spread back to the inside of the runner and finally separated inside the runner and leaf alternately.

**Author Contributions:** Q.L. proposed the innovation ideas and theoretical analysis, and F.Z. carried out experiments and data analysis. L.X. conceived of the study, participated in its design and coordination and helped to draft the manuscript. All authors have read and agreed to the published version of the manuscript.

**Funding:** This project is supported by National Natural Science Foundation of China (Grant No. 52066011). The authors thank State Key Laboratory of Hydropower Equipment (Harbin Institute of Large Electrical Machinery China). Innovation Fund Project of higher education in Gansu Province (Grant No. 2023B-434).

**Conflicts of Interest:** The authors declare no conflict of interest. All data for the paper can be obtained by contacting the corresponding author via email.

## Nomenclature

$\rho$	Fluid density
$k$	Turbulent kinetic energy
$t$	Time
$u$	X-direction velocity
$v$	Y-direction velocity
$w$	Z-direction velocity
$\mu$	Fluid viscosity
$\mu_t$	Turbulent viscosity
$\sigma_k$	Prandtl number corresponding to turbulent kinetic energy
$G_k$	Turbulent kinetic energy due to average velocity gradient
$\sigma_\varepsilon$	Prandtl number corresponding to turbulent dissipation rate
$\varepsilon$	Turbulent dissipation rate

$C_1$	A coefficient related to viscosity
$E$	Shear strain rate
$a_0$	Guide vane opening

## References

- Li, W.; Li, Z.; Qin, Z.; Yan, S.; Wang, Z.; Peng, S. Influence of the solution pH on the design of a hydro-mechanical magneto-hydraulic sealing device. *Eng. Fail. Anal.* **2022**, *135*, 106091. [\[CrossRef\]](#)
- Li, D.; Wang, H.; Qin, Y.; Li, Z.; Wei, X.; Qin, D. Mechanism of high amplitude low frequency fluctuations in a pump-turbine in pump mode. *Renew. Energy* **2018**, *126*, 668–680. [\[CrossRef\]](#)
- Zhang, Y.; Zheng, X.; Li, J.; Du, X. Experimental study on the vibrational performance and its physical origins of a prototype reversible pump turbine in the pumped hydro energy storage power station. *Renew. Energy* **2019**, *130*, 667–676. [\[CrossRef\]](#)
- Fu, X.; Li, D.; Wang, H.; Zhang, G.; Li, Z.; Wei, X. Influence of the clearance flow on the load rejection process in a pump-turbine. *Renew. Energy* **2018**, *127*, 310–321. [\[CrossRef\]](#)
- Yang, J.; Pavesi, G.; Liu, X.; Xie, T.; Liu, J. Unsteady flow characteristics regarding hump instability in the first stage of a multistage pump-turbine in pump mode. *Renew. Energy* **2018**, *127*, 377–385. [\[CrossRef\]](#)
- Li, C.; Zhou, J. Parameters identification of hydraulic turbine governing system using improved gravitational search algorithm. *Energy Convers. Manag.* **2011**, *52*, 374–381. [\[CrossRef\]](#)
- Xiang, K.; Xu, C.; Wang, J. Understanding the Relationship Between Tourists' Consumption Behavior and Their Consumption Substitution Willingness Under Unusual Environment. *Psychol. Res. Behav. Manag.* **2021**, *14*, 483–500. [\[CrossRef\]](#) [\[PubMed\]](#)
- Hasmatuchi, V.; Farhat, M.; Roth, S.; Botero, F.; Avellan, F. Experimental Evidence of Rotating Stall in a Pump-Turbine at Off-Design Conditions in Generating Mode. *J. Fluids Eng.* **2011**, *133*, 051104. [\[CrossRef\]](#)
- Li, D.Y.; Han, L.; Wang, H.J.; Gong, R.Z.; Wei, X.Z.; Qin, D.Q. Flow characteristics prediction in pump mode of a pump-turbine using large eddy simulation. *Proc. Inst. Mech. Eng. Part E J. Process Mech. Eng.* **2017**, *231*, 961–977. [\[CrossRef\]](#)
- Kan, K.; Binama, M.; Chen, H.; Zheng, Y.; Zhou, D.; Su, W.; Muhirwa, A. Pump as turbine cavitation performance for both conventional and reverse operating modes: A review. *Renew. Sustain. Energy Rev.* **2022**, *168*, 112786. [\[CrossRef\]](#)
- Kan, K.; Zhang, Q.; Xu, Z.; Zheng, Y.; Gao, Q.; Shen, L. Energy loss mechanism due to tip leakage flow of axial flow pump as turbine under various operating conditions. *Energy* **2022**, *255*, 124532. [\[CrossRef\]](#)
- Kan, K.; Xu, Z.; Chen, H.; Xu, H.; Zheng, Y.; Zhou, D.; Muhirwa, A.; Maxime, B. Energy loss mechanisms of transition from pump mode to turbine mode of an axial-flow pump under bidirectional conditions. *Energy* **2022**, *257*, 124630. [\[CrossRef\]](#)
- Hongjie, W.; Jianpeng, W.; Ruzhi, G.; Chaoying, S.; Deyou, L.; Xianzhu, W. Investigations on Pressure Fluctuations in the S-Shaped Region of a Pump-Turbine. *Energies* **2021**, *14*, 20.
- Zhang, W.; Chen, Z.; Zhu, B.; Zhang, F. Pressure fluctuation and flow instability in S-shaped region of a reversible pump-turbine. *Renew. Energy* **2020**, *154*, 826–840. [\[CrossRef\]](#)
- Li, R.; Liu, D.; Dong, Z. Numerical simulation of full flow channel in "S" shape zone of pump turbine. *J. Drain. Irrig. Mach. Eng.* **2013**, *31*, 401–405.
- Widmer, C.; Staubli, T.; Ledergerber, N. Unstable Characteristics and Rotating Stall in Turbine Brake Operation of Pump-Turbines. *J. Fluids Eng.* **2011**, *133*, 041101. [\[CrossRef\]](#)
- Klemm, D. Stabilizing the Characteristics of a Pump Turbine in the Range between Turbine Part Load and Reverse Pump Operation. *Voith Res. Constr.* **1982**, *28*, 2.
- Xu, L.; Peng, Y.; Tang, W. Study on flow pattern and pressure pulsation of pump turbine in S characteristic region. *Hydrodyn. Res. Prog. A* **2022**, *37*, 213–225. [\[CrossRef\]](#)
- Li, W.; Li, Z.; Han, W.; Li, Y.; Yan, S.; Zhao, Q.; Gu, Z. Pumping-velocity variation mechanisms of a ferrofluid micropump and structural optimization for reflux inhibition. *Phys. Fluids* **2023**, *35*, 052005.
- Li, W.; Li, Z.; Han, W.; Li, Y.; Yan, S.; Zhao, Q.; Chen, F. Measured viscosity characteristics of Fe<sub>3</sub>O<sub>4</sub> ferrofluid in magnetic and thermal fields. *Phys. Fluids* **2023**, *35*, 012002. [\[CrossRef\]](#)
- Kan, K.; Li, H.; Chen, H.; Xu, H.; Gong, Y.; Li, T.; Shen, L. Effects of Clearance and Operating Conditions on Tip Leakage Vortex-induced Energy Loss in an Axial-Flow Pump Using Entropy Production Method. *J. Fluids Eng.* **2022**, *145*, 031201. [\[CrossRef\]](#)
- Capurso, T.; Stefanizzi, M.; Pascazio, G.; Camporeale, S.M.; Torresi, M. Dependency of the slip phenomenon on the inertial forces inside radial runners. In *AIP Conference Proceedings*; AIP Publishing LLC: Melville, NY, USA, 2019; Volume 2191, p. 020034.
- Suh, J.-W.; Kim, J.-W.; Choi, Y.-S.; Joo, W.-G.; Lee, K.-Y. Development of numerical Eulerian-Eulerian models for simulating multiphase pumps. *J. Pet. Sci. Eng.* **2018**, *162*, 588–601. [\[CrossRef\]](#)
- Agrawal, K.K.; Bhardwaj, M.; Misra, R.; Das Agrawal, G.; Bansal, V. Optimization of operating parameters of earth air tunnel heat exchanger for space cooling: Taguchi method approach. *Geotherm. Energy* **2018**, *6*, 1–17. [\[CrossRef\]](#)
- Peppas, K.P.; Tombras, G.S.; Stassinakis, A.N.; Nistazakis, H.E. Improving the availability of terrestrial fso links over log normal atmospheric turbulence channels using dispersive chirped gaussian pulses. *Opt. Laser Technol.* **2013**, *54*, 329–334.
- Tian, W.; Song, B.; Mao, Z. Conceptual design and numerical simulations of a vertical axis water turbine used for underwater mooring platforms. *Int. J. Nav. Archit. Ocean. Eng.* **2013**, *5*, 625–634.

27. Liu, C. Research on Cavitation Flow Characteristics of Pump Turbine under Partial Load Conditions. Ph.D. Thesis, Lanzhou University of Technology, Lanzhou, China, 2016.
28. Zhang, M.; Montewka, J.; Manderbacka, T.; Kujala, P.; Hirdaris, S. A Big Data Analytics Method for the Evaluation of Ship—Ship Collision Risk reflecting Hydrometeorological Conditions. *Reliab. Eng. Syst. Saf.* **2021**, *213*, 107674. [[CrossRef](#)]

**Disclaimer/Publisher’s Note:** The statements, opinions and data contained in all publications are solely those of the individual author(s) and contributor(s) and not of MDPI and/or the editor(s). MDPI and/or the editor(s) disclaim responsibility for any injury to people or property resulting from any ideas, methods, instructions or products referred to in the content.